Front. Earth Sci. 2023, 17(2): 514–526
https://doi.org/10.1007/s11707-022-1027-9

RESEARCH ARTICLE

Study on fracture characteristics in coal and shale for coal-measure gas reservoir based on 3D CT reconstruction and fractal features

Huijun WANG[1], Shangbin CHEN (✉)[1,2], Shaojie ZHANG[1,2], Chengxing ZHANG[3], Yang WANG[1,2], Gaofeng YI[1], Yixuan PENG[1]

1 School of Resources and Geoscience, China University of Mining and Technology, Xuzhou 221116, China
2 Key Laboratory of Coalbed Methane Resources and Reservoir Formation Process (the Ministry of Education), China University of Mining and Technology, Xuzhou 221116, China
3 School of Earth Sciences and Engineering, Sun Yat-sen University, Guangzhou 510275, China

Abstract Pores and fractures are important components of flow channels in coal-measure gas reservoirs. While considerable studies have been conducted on pore structure evolution, very few studies have investigated the fracture distribution and self-similarity characteristics. To reveal the characteristics of fracture distribution in coal and shale reservoirs, computed tomography studies were performed on 15 coal and shale samples from the Shanxi and Taiyuan formations. The results show that the fracture distribution of samples of the same lithology differs significantly, and the fracture distribution heterogeneity of shale samples is much higher than that of coal samples. In shale, the heterogeneity of fracture distribution is mainly caused by pores and fractures smaller than 2 μm in the *z*-direction, with relatively little contributions from pores and fractures in the *x* and *y* directions. However, the heterogeneity of fracture distribution in coal is mainly controlled by pores and fractures larger than 2 μm in all directions, and the difference between the three directions is minor. It was shown that a great number of microscopic pores and fractures contribute to the highest fractions of porosity in different lithological samples. This method is useful for determining the fracture distribution characteristics in shale and coal-measure gas reservoir.

Keywords pore-fracture system, fracture distribution, directionality, heterogeneity, CT experiment, coal-measure gas reservoirs

1 Introduction

There are a large number of complex pore-fracture structures at different scales in coal-measure gas reservoirs (Fu et al., 2009; Salmachi et al., 2016, 2021; Zhang et al., 2017; Qin et al., 2018), which together with intralaminar flow and interlaminar flow control the seepage characteristics and commingled production efficiency of coal-measure gas reservoirs (Wang et al., 2018; Su et al., 2020). As an important factor determining the productivity of coal-measure gas, the pore-fracture system has carried out many studies on characterization including photoelectric observation (e.g., optical microscopy (OM), transmission electron microscopy (TEM), focus ion beam/scanning electron microscopy (FIB/SEM)) (Nie et al., 2015; Ni et al., 2017a; Zhang et al., 2021), gas adsorption (e.g., low temperature nitrogen/carbon dioxide/methane sorption adsorption (LPN_2/CO_2/CH_4 GA)) (Salmachi and Haghighi, 2012; Zhang et al., 2019; Wang et al., 2022b), fluid intrusion (e.g., mercury intrusion porosimetry (MIP)) (Zhao et al., 2016), and three-dimensional (3D) reconstruction (Yao et al., 2010; Ni et al., 2017b; Sun et al., 2018; Zhao et al., 2018; Wang et al., 2022a). Among all laboratory measurement and characterization techniques, computed tomography (CT) has received particular attention due to its nondestructive properties, 3D visualization and computational power (Yarmohammadtooski et al., 2017; Karimpouli et al., 2020).

Aiming at the problem that the complexity and heterogeneity of pore and fracture structures in coal-measure gas reservoirs are difficult to directly reveal, scholars have introduced fractal theory to reflect the real properties and states of pore-fracture structures (Liu et al., 2015; Wang et al., 2015; Pan et al., 2016; Shi et al., 2018). Hou et al. (2021) discovered that an increasing fracture network complexity and decreasing fracture

Received August 29, 2022; accepted October 20, 2022

E-mail: shangbinchen@163.com

fractal dimension led to an increase in shale permeability using CT and high-resolution scanning electron microscopy (SEM). Wang et al. (2018) quantitatively studied fractures in different bedding plane directions, and considered that the parallel bedding plane direction fracture density and connectivity were higher. Mou et al. (2021) quantitatively characterized fracturing-induced microfracture changes and calculated the permeability changes of microfractures after hydraulic fracturing, and believed that hydraulic fracturing increased the anisotropy of microfractures. Wang et al. (2022a) argued that hydraulic fracturing increased fracture volume and surface area, with low *in situ* stress differences leading to complex fracture networks, and high *in situ* stress differences leading to large-scale, simple fractures.

The above studies are all based on two-dimensional (2D) images, which may lose important information, such as the actual volume distribution of pores (Chen et al., 2017). Therefore, fractal and multifractal pores and fractures in three-dimensional space are more realistic and practical. Thus, this study characterized the pore and fracture structures of coal and shale by combining the CT scanning method, 3D reconstruction of fractures, and 3D fractal dimension. Indicators of complexity, such as pore size distribution and porosity, and their effects were analyzed quantitatively.

2 Experiments and methods

2.1 Sample collection point and sample preparation

The 15 coal samples and shale samples in this study were collected from coal-measure gas reservoirs in the Xishan mining area of Taiyuan city, the Yangquan mining area of Yangquan city, the Qinshui coal field of Jincheng city, and the Datong coalfield of Datong city, all in Shanxi Province (Fig. 1). The coal samples are characterized by low moisture, volatile matter and high fixed carbon contents. The ash content in the tested coal samples ranged from 5.82% to 52.76%, with an average of 19.49%; the volatile matter content ranged from 7.49% to 26.50%, with an average of 10.91%; the fixed carbon content ranged from 37.43% to 86.85%, with an average of 71.65%; and the moisture content was only 0.35%−3.20%, with an average of 1.25%. The total organic matter (TOC) in coal ranges from 51.76% to 90.91%, with an average of 83.27%. The elemental analysis results show that the kerogen type of the shale sample is type III (Table 1). The burial depth of coal-bearing strata in the Shanxi and Taiyuan Formations is generally 600–2000 m, with the majority exceeding 1200 m. The samples were cut into cylinders with diameters of 2.5 cm and 2 cm using a wire cutting machine in the Key Laboratory of Coalbed Methane, Ministry of Education, China University of Mining and Technology, and scanned with a micro-nano CT scanner at the Modern Analysis and Testing Center of China University of Mining and Technology.

2.2 Fracture visualization method based on 3D CT reconstruction

This study selected coal samples from the Shanxi Taiyuan formations as the research object to visualize the structure of pores and fissures inside the coal body and quantitatively define the development degree of pores and fissures in different coal bodies. The porosity and seepage flow of coal are directly influenced by the size and quantity of pores and fractures. Through CT scanning, images with a resolution of 1.5−15 μm were obtained (Table 2), and a 3D visualization model of the pore and fracture structure of coal was established using 3D CT reconstruction technology. Simultaneously, the analysis module of AVIZO can be utilized to quantitatively study the structural properties of pores and fractures. First, the pore structure in coal is represented as an equivalent sphere, and the equivalent pore size represents the size of the pores (Wang et al., 2020a, 2020 b; Safari et al., 2022; Zang et al., 2022).

$$D_{\mathrm{eq}} = \sqrt[3]{\frac{6V_{\mathrm{pore}}}{\pi}}. \tag{1}$$

In Eq. (1), D_{eq} is the equivalent pore size, μm, and V_{pore} is the single pore volume, μm^3. The porosity component is defined as the ratio of the volume of the pore clusters to the overall volume of the coal sample to evaluate the contribution of distinct pore clusters to the total porosity:

$$\varphi_{\mathrm{pore}} = \frac{V_{\mathrm{pc}}}{V}, \tag{2}$$

where φ_{pore} is the porosity, %, V_{pc} is the total pore volume, μm^3, and V is the total volume of the coal sample, μm^3.

3D CT structural reconstruction can be used to provide pore-throat connectivity properties in coal. Using the connected pore extraction module in AVIZO, a connected pore model can be obtained based on a 3D model of coal pores and fractures. The connected pore model runs up and down along a certain coordinate axis, and fluid can flow in the connected interior of the pore model along the coordinate axis. The ratio of connected pore volume to total pore volume is known as connectivity:

$$T_{\mathrm{c}} = \frac{V_{\mathrm{C}}}{V_{\mathrm{P}}}, \tag{3}$$

where T_{c} is the pore throat connectivity ratio, %; V_{C} is the volume of connected pores, μm^3; and V_{P} is the total pore volume, μm^3.

AVIZO software was used to segment the fracture region of interest (ROI) in the continuous two-

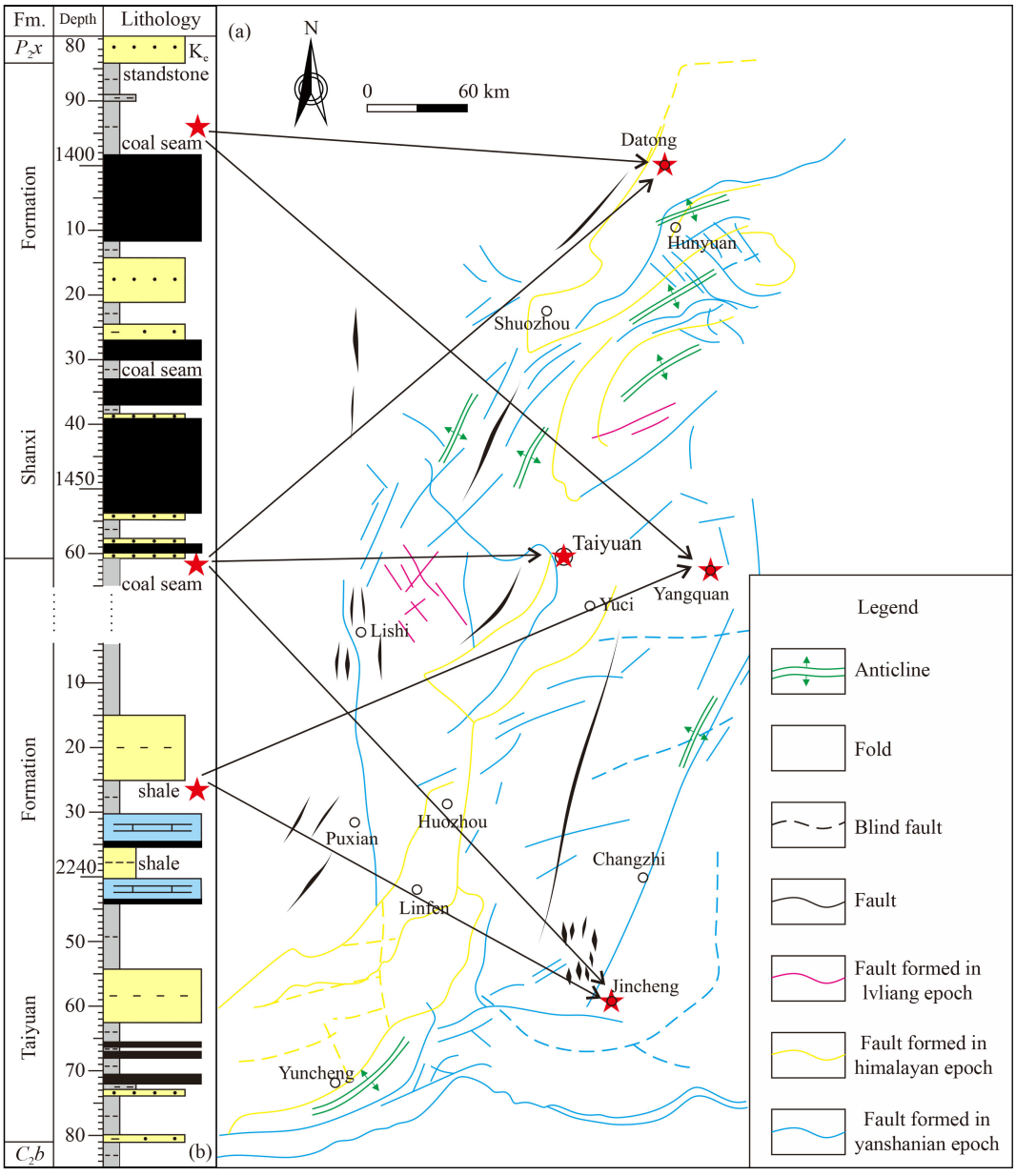

Fig. 1 Structural outline diagram (a) and sampling formation (b). (a) Formation geological period of each structural trace; (b) sampling locations of coal and shale samples used in this study.

Table 1 Element composition and type identification of kerogen in shale samples

Sample ID	TOC/%	Mass fraction/%			Atomic ratio		Type
		C	H	O	H/C	O/C	
Y-10	3.5	54.8	2.10	3.80	0.460	0.052	III
Y-11	3.5	70.7	2.60	3.80	0.441	0.040	III
Y-12	4.8	45.5	1.70	2.50	0.448	0.041	III
Y-13	3.2	46.7	1.80	3.10	0.463	0.050	III
Y-14	3.2	64.5	2.50	3.50	0.465	0.041	III
Y-15	3.3	68.5	2.50	3.70	0.438	0.041	III

dimensional sample slice images obtained from CT experiments (Fig. 2(a)), and the fracture model was then reconstructed (Fig. 2(b)) to generate the three-dimensional pore and fracture structure of the coal. The

Table 2 Voxel resolution and model volume information table

Sample ID	Lithology	TOC	Depth/m	Resolution/μm	ROI number of voxels
Y-1	Coal	83.1	1406.2	1.4546	372 × 368 × 643
Y-2	Coal	85.3	1416.5	1.8989	389 × 327 × 715
Y-3	Coal	89.2	1426.3	1.9352	200 × 200 × 600
Y-4	Coal	80.8	1462.0	1.5495	478 × 406 × 815
Y-5	Coal	84.3	1440.5	1.8989	350 × 350 × 874
Y-6	Coal	82.4	1451.3	1.8989	450 × 450 × 750
Y-7	Coal	85.7	1402.8	1.5578	383 × 418 × 988
Y-8	Coal	90.1	1411.3	1.9102	205 × 197 × 523
Y-9	Coal	86.3	1419.8	2.4006	289 × 281 × 915
Y-10	Shale	3.5	2240.7	15.0897	371 × 394 × 460
Y-11	Shale	3.5	2240.7	15.0897	619 × 611 × 1347
Y-12	Shale	4.8	2239.3	15.3368	743 × 762 × 1039
Y-13	Shale	3.2	2219.2	15.0897	945 × 824 × 944
Y-14	Shale	3.2	2219.2	15.0897	372 × 368 × 643
Y-15	Shale	3.3	1458.3	15.9024	344 × 346 × 506

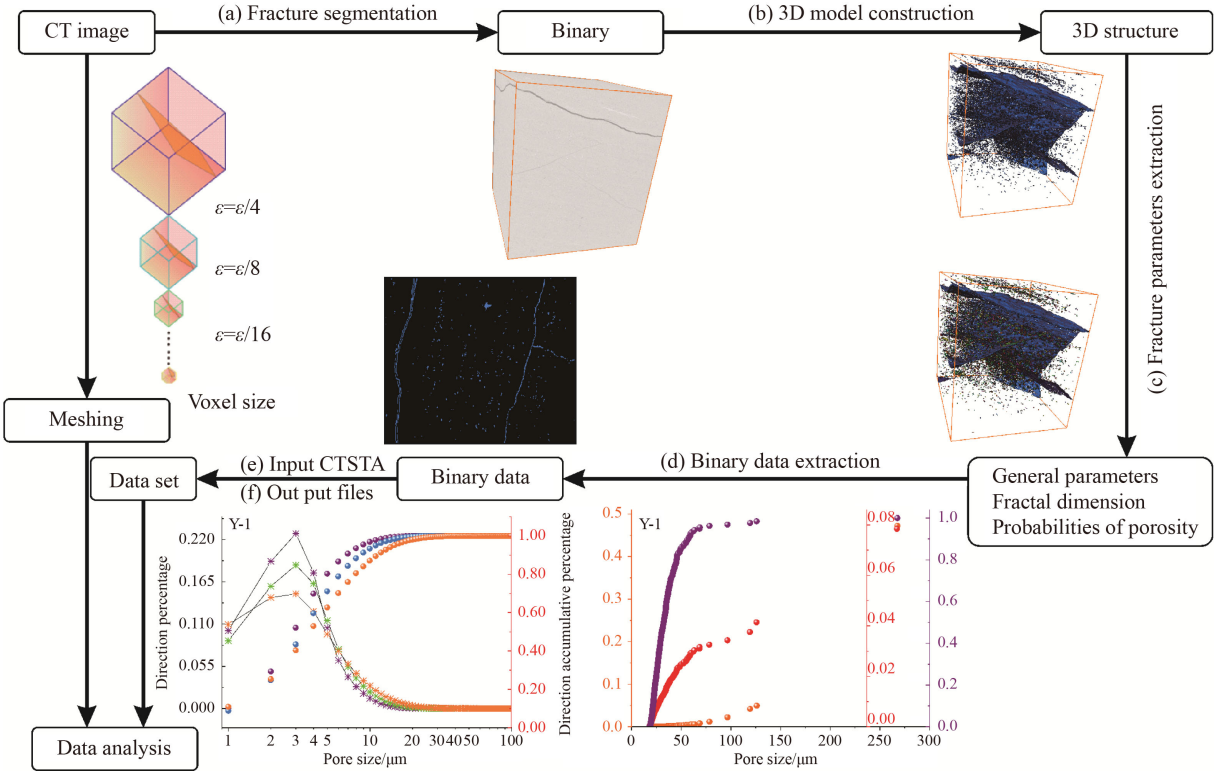

Fig. 2 Schematic diagram of the sample and data processing flow. After the sample has undergone (a) fracture segmentation, (b) 3D model construction, (c) fracture parameter extraction and (d) binary data extraction, the obtained data are input into the CTSTA script for calculation, and the output file contains the pores and cracks required for our analysis and their fractal dimension information.

visual model can extract pore and fracture structure characteristics, such as equivalent pore size (D_{eq}), pore volume (V_{pore}), porosity (φ_{pore}), and total sample volume (V) using the Label analysis module. We exported the binarized pore and fracture structure model, extracted the binarized data of the fracture boundary in the model (Figs. 2(c) and 2(d)), and then passed it through the code independently developed by Liu et al. (2013, 2016). CTSTA calculates the 3D structure (Fig. 2(e)) and generates ten result files, as shown in Fig. 2(f) (all the

calculation result data for the 3D model of sample Y-1). The 3D fractal and quantitative analyses, such as fracture composition analysis, were performed using these data (Fig. 2(e)).

2.3 Calculation method of the 3D fractal dimension of a fracture

The Hausdorff-Besicovitch dimension, proposed by the German mathematician Felix Hausdorff in 1918, is used to calculate the three-dimensional fractal dimension (Xie , 1996; Guo et al., 2015). A subset of any metric space can have its dimension defined by numbers. An x-coordinate and a y-coordinate must be defined to describe a point in a plane. The plane's dimension then is two. This concept's mathematical model is comparable to the topological dimension. The topological dimension must be a natural number. The Hausdorff dimension is identical to the typical geometric or topological dimension for simple geometric structures such as lines, rectangles, and cuboids. When describing irregular sets, however, the Hausdorff method needs to be used. In general, unlike the topological dimension, the Hausdorff dimension of an object is not always a natural number but can also be a nonintegral rational number or irrational integer.

N is the smallest number of spheres of radius R that must be used to cover all points in a set of finite sizes in three-dimensional space. Then N, the lowest number, is a function of R. When N approaches 0, the Hausdorff dimension d is shown as follows:

$$d = -\lim_{R\to 0} \log_R N. \tag{4}$$

The appropriate corresponding n-dimensional objects should be used in n-dimensional space. The number of "spheres" required for a curve of finite length is inversely proportional to its radius; hence, the Hausdorff dimension of the curve is 1. The number of "spheres" required for a plane is obviously inversely proportional to the square of its radius, so the Hausdorff dimension of this plane is 2. However, calculating the Hausdorff dimension directly is challenging. In general, the box-counting dimension can estimate the upper bound, whereas the local dimension or the local dimension can estimate the lower bound. The box-counting dimension can be regarded as placing an object to be fractal in a uniformly divided network; at least a few grids are required to cover the fractal object, and the number of grids needed is estimated by gradually refining the grid (Fig. 3), thereby calculating the box-counting dimension.

Typically, the grid side length is assumed to be ε, the space is divided into N grids with side lengths of ε, and the box dimension is

$$\dim_{\text{box}}(S) = \lim_{\varepsilon\to 0} \frac{\log N(\varepsilon)}{\log(1/\varepsilon)}. \tag{5}$$

The grid used to calculate the box dimension can be square or circular. The advantage of using a sphere with a radius of ε to cover the space is that it is easier to apply to more general problems than the mathematical form of a square. The advantage of utilizing a square to cover the space in the distance space is that it is easier to calculate $N(\varepsilon)$, and the number of boxes and its covering number are equal. For the same covering number, more balls are needed. To facilitate the calculation, the three-dimensional fractal dimensions of the cracks are calculated using box-counting dimensions. The grid is used to cover the fracture, and the side length of the grid is doubled from the voxel size to the ROI. The slope is calculated by the logarithmic ratio of the number of grids occupied by the fractal object to the side length of the grid, and this slope of the fitted straight line is the fractal dimension of the three-dimensional object.

3 Results and discussion

3.1 Visual characterization and quantitative characterization of pores and fractures of samples

The 3D CT structure reconstruction procedure is shown

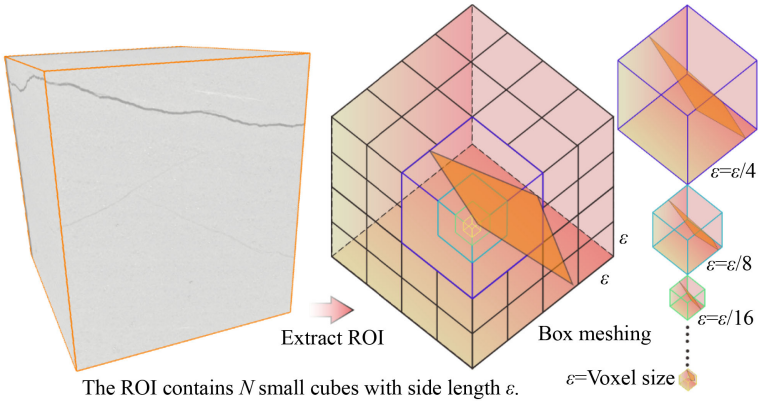

Fig. 3 Schematic diagram of box-counting dimension division. The extracted ROI is divided into cubes with different side lengths for calculation.

in Fig. 4(a). The range of interest (ROI) is chosen first. For CT scanning, the higher the brightness in the image, the higher its density. The mineral pyrite has the highest density and the smallest pore and fracture density. Pyrite and pores and fissures can be extracted separately using this principle. Then, as illustrated in Figs. 4(b) and 4(c), it can be rendered based on the voxel size to obtain the characteristics of pores and fissures in each coal sample, and the evaluations of the pore change laws in the x, y, and z directions are shown in Fig. 5(a). The coal samples

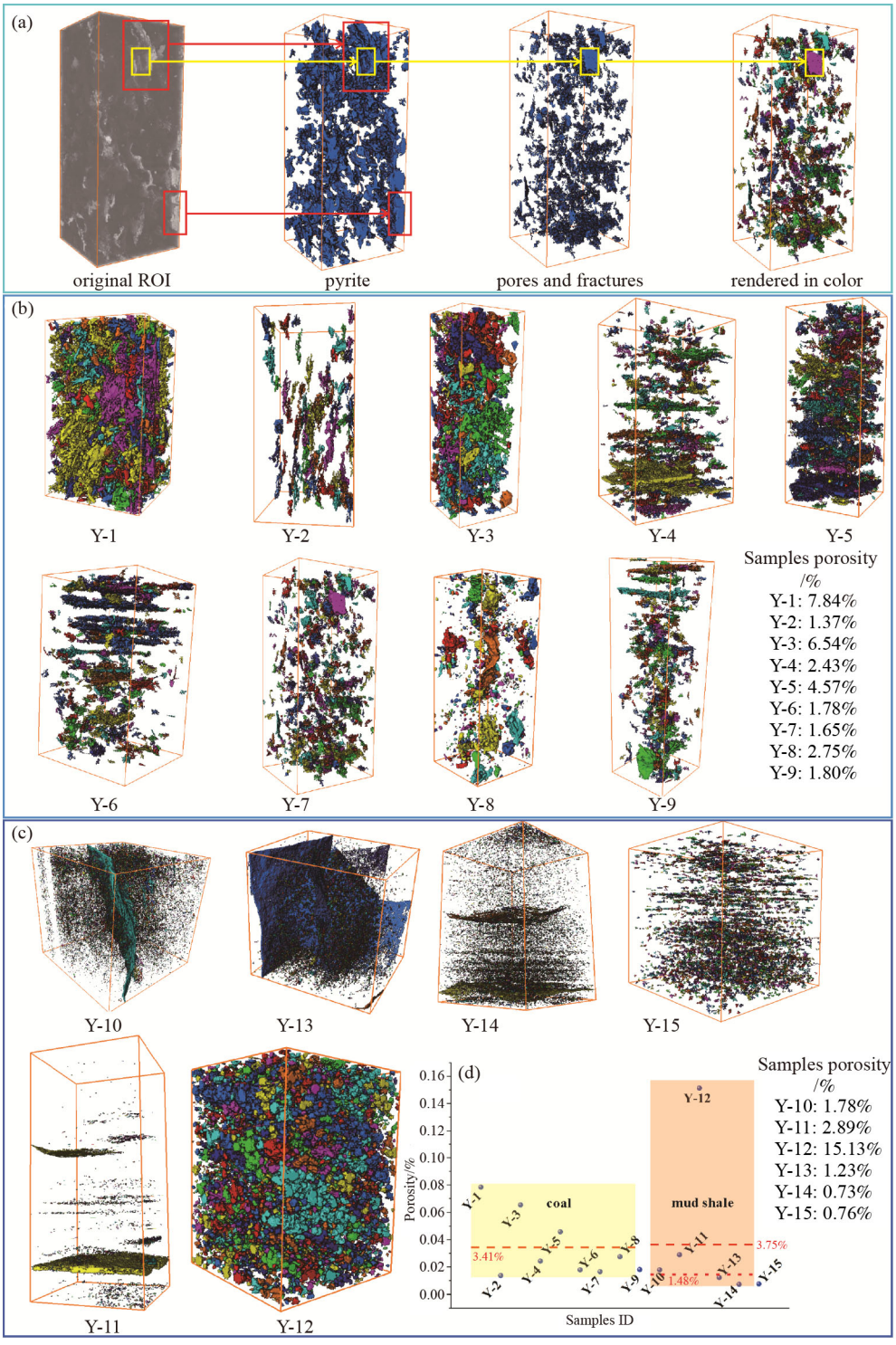

Fig. 4 Schematic diagram of pore and fracture visualization process and result display. The CT processing process of the sample includes (a) selecting the ROI; (b) extracting mineral components; (c) extracting pores and cracks; and (d) rendering pores and cracks.

in Fig. 4(b) have pores and fractures that are characterized by a large number of pores and very few fractures. As shown in Fig. 4(d), the porosities of samples Y-1 to Y-9 are 7.84%, 1.37%, 6.54%, 2.43%, 4.57%, 1.78%, 1.65%, 2.75%, and 1.8%, respectively, with an average porosity of approximately 3.41%. The samples in Fig. 4(c) are all shale samples, their pores and fissures are characterized by a high density of fractures, and only a certain number of pores are observed between fractures. As shown in Fig. 4(d), the porosities of samples Y-10 to Y-15 are 1.78%, 2.89%, 15.13%, 1.23%, 0.73%, and 0.76%, respectively, with an average porosity of 3.75%. Sample Y-12 has no fractures, and the average porosity of the other samples is approximately 1.48%, indicating that the shale samples were generally less pore than the coal samples. Furthermore, the development of pores and fractures in coal and shale samples has a layered distribution feature, which is consistent with the bedding phenomenon in macroscopic observations of those samples. The pore size contributions of the coal sample and the shale sample are compared by evaluating the pore size variance in the *x*, *y*, and *z* directions. The scatter plot in Fig. 5(b) demonstrates that the pore sizes of those shale samples generally reach a maximum direction accumulative value of approximately 20 μm (scatter plot in Fig. 5(b)), confirming the abovementioned pore and fracture development features. In coal and shale samples, pores and fractures with sizes below 10 μm have the largest porosity contribution, and the peaks mostly appear at 2 μm. However, pore size contributions in the *x*, *y*, and *z* directions for each sample showed significant differences. For example, the pores of samples Y-10 and Y-15 are dominated by pores and cracks with a diameter of 1 μm in the *z* direction, while samples Y-11, Y-12, and Y-13 have a large number of pores and cracks of 2 μm in the *z*, *z*, and *x* directions, respectively. Similar phenomena have been observed in coal samples, indicating that the directionality of the pore size contribution is potentially independent of the lithology. Combining the cumulative pore size components (purple points) in Fig. 6, it can be seen that in both the coal and shale samples, when the pore size is small, the porosity quickly reaches the maximum value; the cumulative porosity (red points) also shows the same trend; and the porosity component (orange points) also exhibits a highly dense distribution of data points at low values for this sample, indicating that the porosity is mainly contributed by pores and fractures with smaller sizes (Xu et al., 2022).

3.2 Characteristics of the 3D fractal dimension of fracture distribution

Table 3 shows the logarithmic values of the lattice side length and the lattice number based on the method stated in Section 2.2, and Fig. 7 shows the trend lines for the 3D fractal dimension based on these values. The results suggest that the mean fractal dimension of the nine coal samples is 2.3579, the standard deviation is 0.2234, and the variance is 0.0499. The mean value of the fractal dimension for these six shale samples is approximately 2.5772, the standard deviation is 0.2509, and the variance is 0.06295. The mean value suggests that the internal heterogeneity of the shale sample is slightly higher than that of the coal sample (Li et al., 2022), and the standard deviation indicates that the distributions of fractures in those samples of the same lithology are significantly different. This feature is visualized in Fig. 4(b) and Fig. 4(c). The fractal dimensions of the 15 samples are shown in Table 3. The coal samples have fractal dimensions between 2.4 and 2.5, while the shale samples have values between 2.6 and 2.9. The fractal dimension values can be used to depict the distribution of fractures in samples, and they indicate that the distribution of pores and fractures in the coal samples is relatively uniform. Figure 8 shows that shale samples are largely concentrated in the upper half of the *y*-*z* plane and the upper right part of the *x*-*z* plane, supporting this conclusion. By comparing the differences in fractal dimension of various lithologic samples longitudinally and combining analyses of the pore size contribution in Section 3.1, it can be concluded that shale has higher heterogeneity than coal, the heterogeneity is primarily caused by pores smaller than 2 μm in the *z*-direction (Fig. 5(a)), and the pores and fractures in the *x* and *y* directions have relatively little influence on heterogeneity. While the combined impacts of the *z*-direction and pores and fractures greater than 2 μm in the *x* and *y* directions generate heterogeneity in coal (Fig. 5(b)), the differences in the three directions are minor.

3.3 Analysis of fracture distribution tendency

The microscopic and independent system composed of pores and fissures can be observed via 3D visualization. Corresponding to the relationships between the pores and the beddings, it is expected that the microcosm will have characteristics of pores and fissures that are essentially parallel to the bedding, as shown intuitively in Fig. 4. This may be due to the special structural and mechanical characteristics endowed by the diagenetic process and tectonic evolution. Chen et al. (2022) characterized the fracture development of coal reservoirs after low-pressure water injection through water injection experiments and CT methods. Liu et al. (2021) proposed a porosity calculation method based on NMR and CT three-dimensional reconstruction techniques. They both concluded that the larger the pore size is, the smaller the number of pores, and the larger the porosity component,

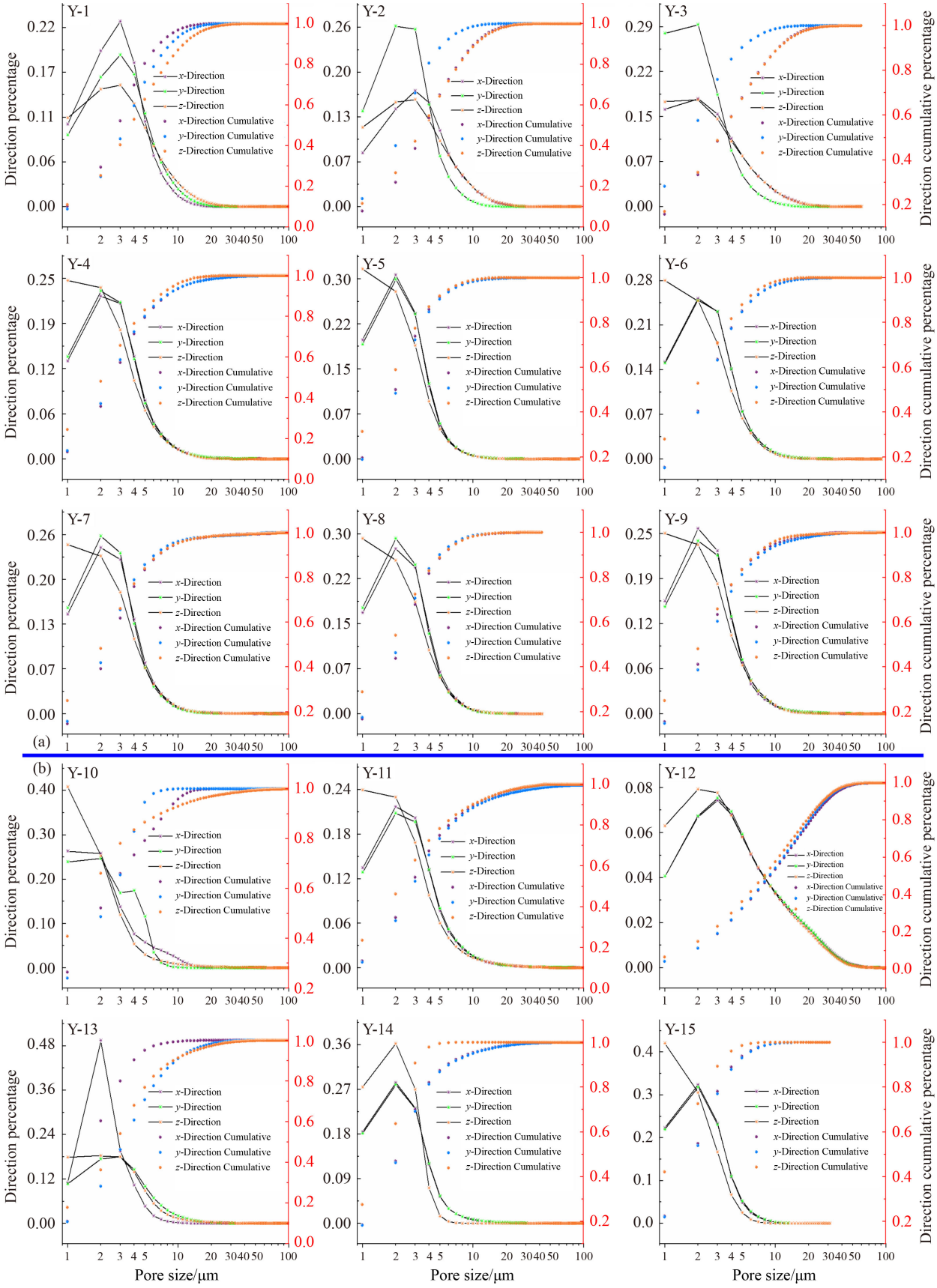

Fig. 5 Porosity contribution and porosity accumulation curve in the *x*, *y*, *z* directions.

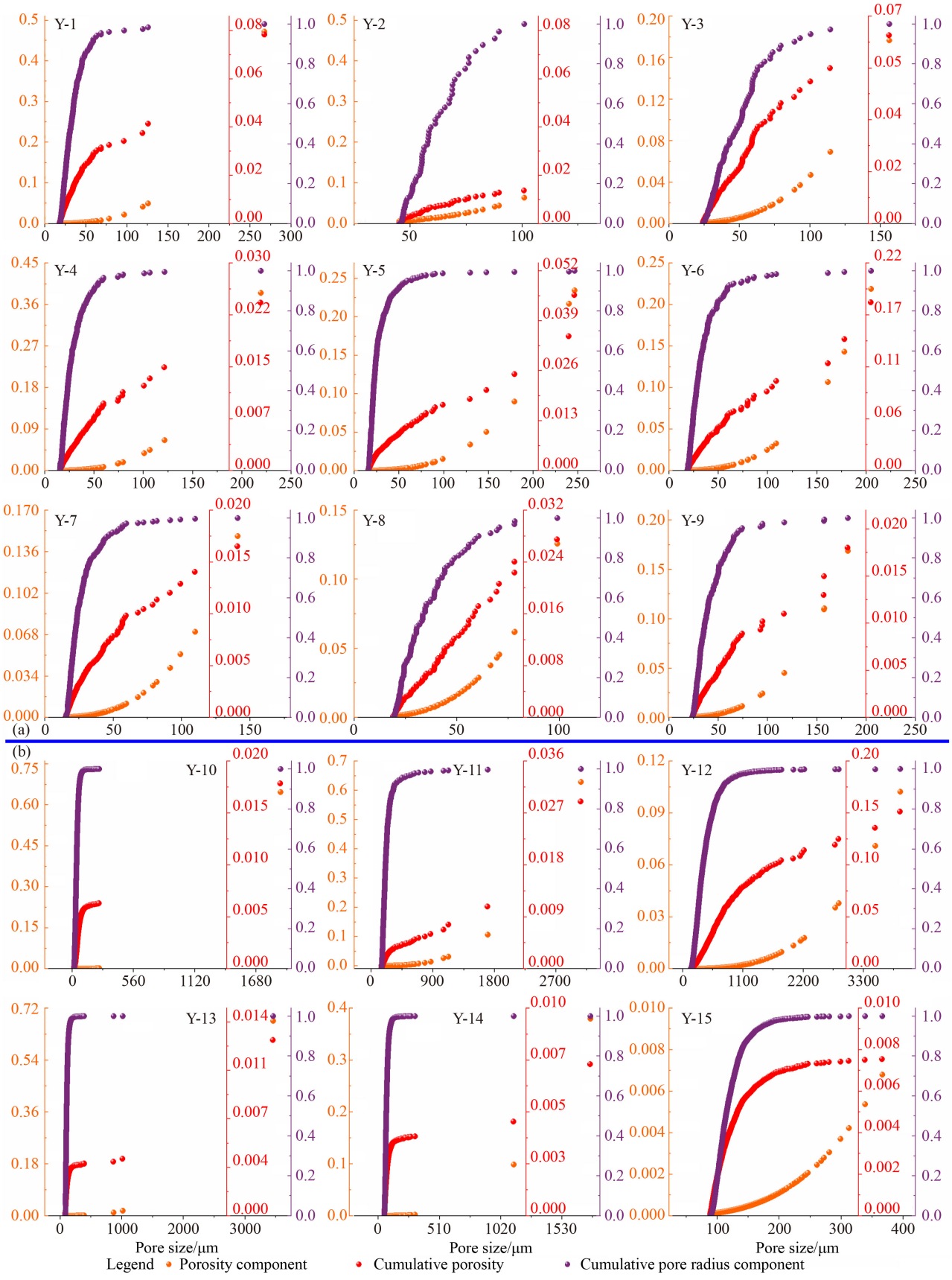

Fig. 6 Porosity component and its cumulative pore radius component.

Table 3 The number of grids and the logarithm of grid side length

Y-1		Y-2		Y-3		Y-4		Y-5	
Fractal dimension		Fractal dimension		Fractal dimension		Fractal dimension		Fractal dimension	
2.20268		2.44193		2.13249		2.27559		2.52048	
log(1/ε)	log*N*(ε)	log(1/ε)	log*N*(ε)	log(1/ε)	log*N*(ε)	log(1/ε)	log*N*(ε)	log(1/ε)	log*N*(ε)
−1.9758	4.23411	−0.49584	2.70805	−0.75139	2.63906	−0.86436	1.38629	−2.59803	5.45104
−2.1881	4.85981	−0.54759	2.83321	−1.09676	3.55535	−1.52413	2.83321	−2.82802	6.07074
−2.2817	5.0689	−0.7749	3.43399	−1.35	4.06044	−1.80838	3.49651	−3.02537	6.6107
−2.436	5.41165	−0.9847	3.91202	−1.5334	4.36945	−2.12369	4.11087	−3.16202	6.97354
−2.6986	5.96871	−1.03229	4.00733	−1.538	4.38203	−2.34382	4.67283	−3.46478	7.75662
−2.8196	6.21461			−1.6052	4.58497	−2.66528	5.45104	−3.70908	8.37931
−2.8243	6.22851			−1.80205	4.96981	−2.86699	5.93754	−3.93529	8.93879
−3.019	6.55962			−1.80236	4.97673	−2.98796	6.2106	−4.08995	9.31344
				−1.9664	5.26269	−3.03427	6.27099	−4.37803	9.87473

Y-6		Y-7		Y-8		Y-9		Y-10	
Fractal dimension		Fractal dimension		Fractal dimension		Fractal dimension		Fractal dimension	
2.01242		2.74387		2.43728		2.45474		2.60968	
log(1/ε)	log*N*(ε)	log(1/ε)	log*N*(ε)	log(1/ε)	log*N*(ε)	log(1/ε)	log*N*(ε)	log(1/ε)	log*N*(ε)
−1.85925	4.17439	−0.99414	2.99573	−0.34269	2.19722	−0.9459	2.07944	−4.56691	7.99092
−2.11702	4.81218	−1.28118	3.71357	−0.66645	2.94444	−1.41993	3.17805	−4.66386	8.28853
−2.30659	5.21494	−1.45333	4.15888	−0.81245	3.3322	−1.56089	3.7612	−4.78789	8.64611
−2.42509	5.52943	−1.5206	4.34381	−0.94892	3.61092	−1.73194	4.2485	−4.87829	8.90788
−2.59682	5.95064	−1.67089	4.80402	−1.01819	3.82864	−1.94841	4.7362	−4.9879	9.20774
−2.82094	6.34739	−1.85081	5.34711	−1.09491	3.97029	−2.17525	5.22575	−5.12605	9.54438
−3.22038	6.86276	−1.99216	5.68698	−1.21777	4.29046	−2.32524	5.53733	−5.23066	9.77985
				−1.33169	4.65396	−2.51257	5.83481	−5.35172	10.02796
				−1.41787	4.77912				

Y-11		Y-12		Y-13		Y-14		Y-15	
Fractal dimension		Fractal dimension		Fractal dimension		Fractal dimension		Fractal dimension	
2.61626		2.39535		2.75558		2.89323		2.19326	
log(1/ε)	log*N*(ε)	log(1/ε)	log*N*(ε)	log(1/ε)	log*N*(ε)	log(1/ε)	log*N*(ε)	log(1/ε)	log*N*(ε)
−1.62587	2.48491	−0.48652	1.38629	−4.29255	7.29912	−3.9649	6.43615	−1.18446	5.31321
−2.12201	3.52636	−1.10673	2.89037	−4.35831	7.58528	−3.96595	6.44731	−1.41969	6.3081
−2.44392	4.35671	−1.34144	3.3673	−4.37327	7.64779	−3.97124	6.4552	−1.6145	7.05618
−2.66628	4.97673	−1.60714	4.04305	−4.55733	8.36939	−3.97709	6.47389	−1.73443	7.46107
−2.81491	5.47227	−1.76709	4.40672	−4.57658	8.44741	−3.98245	6.49224	−1.9163	8.00169
−2.93916	5.86079	−1.90508	4.72739	−5.01464	9.49582	−3.98944	6.50578	−2.22405	8.55082
−3.09533	6.29895	−2.07776	5.15906	−5.19216	9.6303	−3.99269	6.52062	−2.53818	8.80387
−3.24189	6.62804	−2.17507	5.4161	−5.28837	9.67263	−3.99758	6.53524	−2.80462	8.97487
−3.42898	6.99760								

which is similar to our conclusion. Some quantitative characterizations of the distribution trend of pores and fissures were acquired by the calculation of the 3D structure. While the porosity accumulation curves of coal samples reach a maximum value at less than 10 μm, the porosity accumulation curves of shale samples reach a maximum value at approximately 20 μm. The pores and fractures less than 10 μm contribute the most porosity in both coal and shale samples, peaks appear at 2 μm, and there is no consistent pattern in the contribution of pores of different sizes in different directions for each sample. Since there is no instrument that can reliably and

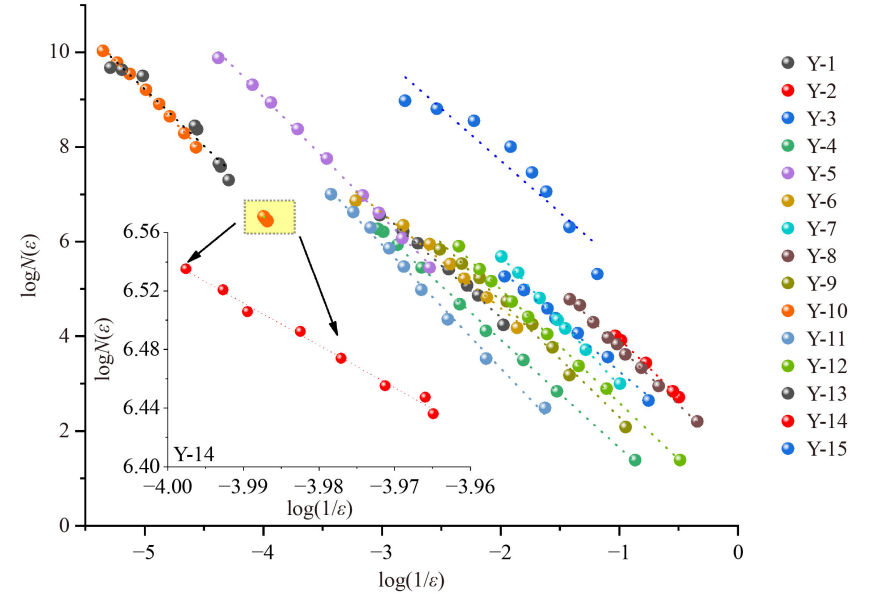

Fig. 7 Fitting results of fracture fractal dimensions.

intuitively observe the nanometer or even molecular level, we believe that the value of 2 m may be constrained by the accuracy of the experimental apparatus. Therefore, in subsequent studies, we plan to use molecular simulations to investigate the potential causes of this value. Porosity is an important numerical index for measuring the degree of development of pores and fractures, and the fractal dimension is an essential numerical index for measuring internal self-similarity. The heterogeneity of the distribution of pores and fractures in shale samples is dominated by pores and fractures smaller than 2 μm in the z direction. Pores and fractures in the x and y directions produce very little heterogeneity in shale, whereas they contribute significantly more heterogeneity in coal. This is due to the effect of pores and fissures larger than 2 μm in all directions, with negligible changes across the three directions, suggesting that coal heterogeneity is lower than shale heterogeneity. Figure 9 depicts a degree of symmetry between the numerical index and the porosity, but it is clear that this symmetry is not about a straight line acting as the symmetry axis, and its symmetry will be

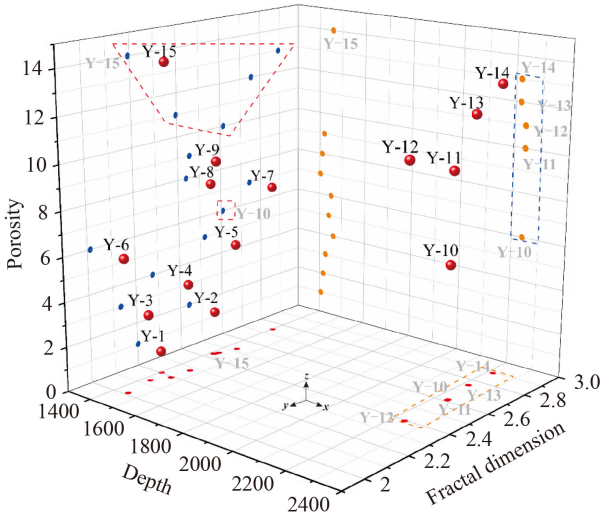

Fig. 8 The 3D scatter plot of sample burial depth, porosity and fracture fractal dimension.

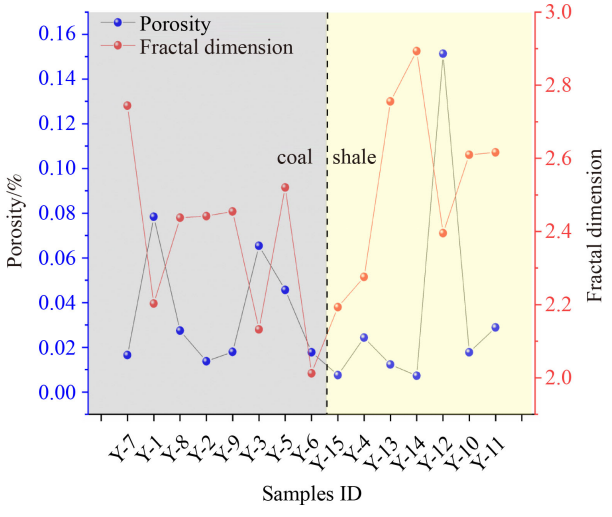

Fig. 9 Variation trends of fractal dimension and porosity for coal and shale samples.

steadily deepened in our further studies.

4 Conclusions

This study provides a new method for evaluating the distribution characteristics of fractures combining CT scanning, 3D visualization, and reconstruction of pores and fissures, the CTSTA numerical calculation and 3D fractal dimension calculation methods.

1) The pore-fracture system of coal has more pores and fewer fractures, and the growth of both pores and fractures has layered distribution characteristics. Shale fractures have high-density features.

2) Porosity below 10 μm contributes the most, and the peak typically occurs at 2 μm. The pore size of shale samples typically achieves the greatest cumulative value in the direction of approximately 20 μm. The pore size contributions in the *x*, *y*, and *z* directions, however, are considerably different for each sample, indicating that the pore size contributions' directionality may not be correlated to lithology.

3) The pores smaller than 2 μm in the *z*-direction inside the shale samples lead to the heterogeneous distribution of the shale pore-fracture system compared to the coal samples. The standard deviation of the fractal dimension value indicates that the same rock has a significant difference in the distribution of fractures in the samples with high quality, but the difference between the *z* direction and the *x* and *y* directions is very small.

We discover that there is some symmetry between the fractal dimension value and the porosity of different samples, but it is not based on a straight line as the axis of symmetry. Its symmetry parameters will be investigated in our follow-up work.

Acknowledgments This study was supported by the National Natural Science Foundation of China (Grant Nos. 41972171 and 42172156), the Fundamental Research Funds for the Central Universities (No. 2020CXNL11), the Graduate Innovation Program of China University of Mining and Technology (No. KYCX22_2604), and the Priority Academic Program Development of Jiangsu Higher Education Institutions (PAPD).

References

Chen J, Cheng W, Wang G, Li H M (2022). Effect of dominated coal pores and fractures on water migration after low-pressure water injection based on CT images. Fuel, 307: 121795

Chen X J, Yao G Q, Cai J C, Huang Y T, Yuan X Q (2017). Fractal and multifractal analysis of different hydraulic flow units based on micro-CT images. J Nat Gas Sci Eng, 48: 145–156

Fu X H, Qin Y, Wang G, Rudolph V (2009). Evaluation of coal structure and permeability with the aid of geophysical logging technology. Fuel, 88(11): 2278–2285

Guo L, Ru Z, Xiao-Lian X U, Zhang Y F (2015). CT image reconstruction of coal rock three-dimensional fractures and body fractal dimension under triaxial compression test. Rock Soil Mech, 36(6): 1633–1642 (in Chinese)

Hou P, Liang X, Zhang Y, He J, Gao F, Liu J (2021). 3D multi-scale reconstruction of fractured shale and influence of fracture morphology on shale gas flow. Nat Resour Res, 30(3): 2463–2481

Karimpouli S, Tahmasebi P, Ramandi H L (2020). A review of experimental and numerical modeling of digital coalbed methane: imaging, segmentation, fracture modeling and permeability prediction. Int J Coal Geol, 228: 103552

Li X Y, Chen S B, Wang Y W, Zhang Y K, Wang Y, Wu J F, Zhang J J, Khan J (2022). Influence of pore structure particularity and pore water on the occurrence of deep shale gas: Wufeng–Longmaxi Formation, Luzhou Block, Sichuan Basin. Nat Resour Res, 31(3): 1403–1423

Liu J, Pereira G G, Liu Q B, Regenauer-Lieb K (2016). Computational challenges in the analyses of petrophysics using microtomography and upscaling: a review. Comput Geosci, 89: 107–117

Liu J, Regenauer-Lieb K, Hines C, Zhang S, Bourke P, Fusseis F, Yuan D A (2013). Applications of Microtomography to Multiscale System Dynamics: Visual-isation, Characterisation and High-performance Computation. Berlin: Springer, 653–674

Liu W, Wang G, Han D Y, Xu H, Chu X Y (2021). Accurate characterization of coal pore and fissure structure based on CT 3D reconstruction and NMR. J Nat Gas Sci Eng, 96: 104242

Liu X J, Xiong J, Liang L X (2015). Investigation of pore structure and fractal characteristics of organic-rich Yanchang formation shale in central China by nitrogen adsorption/desorption analysis. J Nat Gas Sci Eng, 22: 62–72

Mou P W, Pan J N, Wang K, Wei J, Yang Y H, Wang X L (2021). Influences of hydraulic fracturing on microfractures of high-rank coal under different *in-situ* stress conditions. Fuel, 287: 119566

Ni X M, Chen W X, Li Z Y, Gao X (2017a). Reconstruction of different scales of pore-fractures network of coal reservoir and its permeability prediction with Monte Carlo method. Int J Min Sci Technol, 27(4): 693–699

Ni X M, Miao J, Lv R S, Lin X Y (2017b). Quantitative 3D spatial characterization and flow simulation of coal macropores based on μCT technology. Fuel, 200: 199–207

Nie B S, Liu X F, Yang L L, Meng J Q, Li X C (2015). Pore structure characterization of different rank coals using gas adsorption and scanning electron microscopy. Fuel, 158: 908–917

Pan Z J, Wang K, Hou Q L, Niu Q H, Wang H T, Ji Z M (2016). Micro-pores and fractures of coals analyzed by field emission scanning electron microscopy and fractal theory. Fuel, 164: 277–285

Qin Y, Moore T A, Shen J, Yang Z B, Shen Y L, Wang G (2018). Resources and geology of coalbed methane in China: a review. Int Geol Rev, 60(5–6): 777–812

Safari H, Faramarzi-Palangar M, Hashemi S M H, Neisarifam O, Sedaee B (2022). A new approach to 3D saturation height modeling by coupling a capillary pressure model with pore throat size distribution. Nat Resour Res, 31(2): 1045–1059

Salmachi A, Haghighi M (2012). Temperature effect on methane sorption and diffusion in coal: application for thermal recovery from coal seam gas reservoirs. APPEA J, 52(1): 291–300

Salmachi A, Rajabi M, Reynolds P, Yarmohammadtooski Z, Wainman C (2016). The effect of magmatic intrusions on coalbed methane reservoir characteristics: a case study from the Hoskissons coalbed, Gunnedah Basin, Australia. Int J Coal Geol, 165: 278–289

Salmachi A, Rajabi M, Wainman C, Mackie S, Mccabe P, Camac B, Clarkson C (2021). History, geology, *in situ* stress pattern, gas content and permeability of coal seam gas basins in Australia: a review. Energies, 14(9): 2651

Shi X H, Pan J N, Hou Q L, Jin Y, Wang Z Z, Niu Q H, Li M (2018). Micrometer-scale fractures in coal related to coal rank based on micro-CT scanning and fractal theory. Fuel, 212: 162–172

Su X B, Li F, Su L N, Wang Q (2020). The experimental study on integrated hydraulic fracturing of coal measures gas reservoirs. Fuel, 270: 117527

Sun Y F, Zhao Y X, Yuan L (2018). Quantifying nano-pore heterogeneity and anisotropy in gas shale by synchrotron radiation nano-CT. Microporous Mesoporous Mater, 258: 8–16

Wang G, Han D Y, Jiang C H, Zhang Z Y (2020a). Seepage characteristics of fracture and dead-end pore structure in coal at micro-and meso-scales. Fuel, 266: 117058

Wang G, Han D Y, Qin X J, Liu Z, Liu J F (2020b). A comprehensive method for studying pore structure and seepage characteristics of coal mass based on 3D CT reconstruction and NMR. Fuel, 281: 118735

Wang M, Xue H T, Tian S S, Wilkins R W T, Wang A W (2015). Fractal characteristics of upper Cretaceous lacustrine shale from the Songliao Basin, NE China. Mar Pet Geol, 67: 144–153

Wang X L, Pan J N, Wang K, Mou P W, Li J X (2022a). Fracture variation in high-rank coal induced by hydraulic fracturing using X-ray computer tomography and digital volume correlation. Int J Coal Geol, 252: 103942

Wang Z K, Gao F, Cai C Z, Su S J, Du M L (2022b). Study on coal seam damage caused by liquid nitrogen under different ground temperature conditions. J Energy Resour Technol, 144(7): 072302

Wang Z Z, Pan J N, Hou Q L, Yu B S, Li M, Niu Q H (2018). Anisotropic characteristics of low-rank coal fractures in the Fukang mining area, China. Fuel, 211: 182–193

Xie H P (1996). Fractal-Introduction to Rock Mechanics. Beijing: Science Press

Xu S, Yang Z, Wu S, Wang L, Wei W, Yang F, Cai J (2022). Fractal analysis of pore structure differences between shale and sandstone based on the nitrogen adsorption method. Nat Resour Res, 31(3): 1759–1773

Yao Y B, Liu D M, Cai Y D, Li J Q (2010). Advanced characterization of pores and fractures in coals by nuclear magnetic resonance and X-ray computed tomography. Sci China Earth Sci, 53(6): 854–862

Yarmohammadtooski Z, Salmachi A, White A, Rajabi M (2017). Fluid flow characteristics of Bandanna Coal Formation: a case study from the Fairview Field, eastern Australia. Aust J Earth Sci, 64(3): 319–333

Zang Q B, Liu C L, Awan R S, Yang X Y, Lu Z D, Li G X, Wu Y P, Feng D H, Ran Y (2022). Comparison of pore size distribution, heterogeneity and occurrence characteristics of movable fluids of tight oil reservoirs formed in different sedimentary environments: a case study of the Chang 7 Member of Ordos Basin, China. Nat Resour Res, 31(1): 415–442

Zhang J J, Wei C T, Yan G Y, Lu G W (2019). Structural and fractal characterization of adsorption pores of middle–high rank coal reservoirs in western Yunnan and eastern Guizhou: an experimental study of coals from the Panguan syncline and Laochang anticline. Energy Explor Exploit, 37(1): 251–272

Zhang S J, Sang Q, Dong M Z (2021). Experimental study of pressure sensitivity in shale rocks: effects of pore shape and gas slippage. J Nat Gas Sci Eng, 89: 103885

Zhang X D, Du Z G, Li P P (2017). Physical characteristics of high-rank coal reservoirs in different coal-body structures and the mechanism of coalbed methane production. Sci China Earth Sci, 60(2): 246–255

Zhao J L, Xu H, Tang D Z, Mathews J P, Li S, Tao S (2016). Coal seam porosity and fracture heterogeneity of macrolithotypes in the Hancheng Block, eastern margin, Ordos Basin, China. Int J Coal Geol, 159: 18–29

Zhao Y X, Sun Y F, Liu S M, Chen Z W, Yuan L (2018). Pore structure characterization of coal by synchrotron radiation nano-CT. Fuel, 215: 102–110